

# Amphiphilic Janus Particles for Aerobic Alcohol Oxidation in Oil Foams

Kang Wang,<sup>1</sup> Josh Davies-Jones,<sup>1</sup> Arthur Graf,<sup>1</sup> Marina Carravetta,<sup>2</sup> Philip R. Davies,<sup>1</sup> Marc Pera-Titus<sup>1\*</sup>

<sup>1</sup> Cardiff Catalysis Institute, School of Chemistry, Cardiff University, Main Building, Park Place, Cardiff CF10 3AT, UK

<sup>2</sup> School of Chemistry, University of Southampton, Highfield, SO17 1BJ, Southampton, UK

*Supporting Information Placeholder*

**ABSTRACT:** Amphiphilic Janus silica particles tunable with oleophobic-oleophilic properties and low fluorine content (8wt%F) exhibited prominent foamability for a variety of aromatic alcohols at low particle concentration (<1 wt%) compared to randomly functionalized silica particles. When selectively loaded with Pd nanoparticles on the oleophilic hemisphere, the particles displayed more than two-fold increase of catalytic activity in the aerobic oxidation of benzyl alcohol compared to non-foam bulk catalysis at ambient O<sub>2</sub> pressure. Particles were conveniently recycled with high foamability and catalytic activity maintained for at least 5 consecutive runs.

**KEYWORDS:** Janus particles, gas-liquid-solid interface, alcohol oxidation, oil foams, microreactor, photo-induced force microscopy (PiFM)

## 1. INTRODUCTION

Liquid foams are omnipresent in our everyday life and are widely used in the formulation of food and beverages, cosmetics, health-care and homecare products, as well as in fire extinguishing, froth flotation and for manufacturing porous materials.<sup>1-4</sup> Foams are typically stabilized using either surfactants, surface-active polymers, or globular proteins.<sup>5-8</sup> These stabilizers exhibit efficacy solely within an aqueous environment and can hardly be applied to organic solvents owing to their low surface tension (typically from 14 to 50 mN·m<sup>-1</sup>). The generation of non-aqueous foams requires stabilizers with low surface energy (*e.g.*, fluorinated surfactants, asphaltenes, fatty acid crystals),<sup>9-12</sup> being as a result much more challenging compared to aqueous foams.

Particles can adsorb at the gas-oil interface and generate ‘armored’ foams in organic solvents preventing the coalescence of gas bubbles and drainage of the liquid phase.<sup>13</sup> To adsorb at the gas-oil interface, particles need: (1) to be overall oleophilic to disperse in the solvent before foaming; (2) a balanced surface density and distribution of oleophilic and oleophobic (aerophilic) groups to adjust the interfacial contact angle within a stability window;<sup>14</sup> and (3) a controlled size to diffuse fast from the bulk liquid to the interface. Few low-surface energy particles can meet concomitantly these three requirements, containing mainly a high surface density of

fluorocarbon chains (*e.g.*, fluoropolymers/ oligomers,<sup>15-17</sup> fluorocarbon chains,<sup>18-21</sup> highly hydrophobic low-carbon chains<sup>22</sup>) in a randomly distributed fashion. This limited scope arises from the low surface tension of organic solvents restricting particle adsorption at the gas-oil interface.<sup>23</sup>

Janus particles (JPs) are a class of anisotropic colloidal particles that possess different chemical composition (and opposing wettability) on each hemisphere.<sup>24-28</sup> This amphiphilic nature allows JPs to adsorb much more strongly at the water-oil interface (up to 3-fold increase of detachment energy) compared to randomly functionalized counterparts due to much lower liquid-particle surface tensions.<sup>29-32</sup> As a result, JPs can generate emulsions, where the interfacial particle self-assembly, orientation and droplet morphology can be governed by the type and density of functional groups on each hemisphere,<sup>33</sup> and by the particle shape and architecture (*e.g.*, spherical, cubic, icosahedral, nano-sheets, dumbbell, mushroom-like).<sup>34-40</sup> These properties make JPs excellent candidates to engineer biphasic catalytic reactions at the water-oil interface by carefully locating catalytic centers either on the water or oil sides of the interface.<sup>41,42</sup> JPs with catalytic centers located at the hydrophobic hemisphere are suitable for reactions in oil phases including organic synthesis<sup>43-48</sup> and desulfurization.<sup>49</sup> In contrast, JPs with catalytic centers located at the hydrophilic hemisphere can promote dye decomposition,<sup>50-53</sup> and photocatalytic water splitting.<sup>54,55</sup> JPs can also be employed to design interfacial catalysts with spatial isolation of acid and basic centers that promoted acid-base tandem reactions.<sup>56</sup>

Despite the significant progress of JPs for stabilizing emulsions, the use of JPs to generate foams has been seldom explored. JPs consisting of a hydrophilic hemisphere incorporating OH / NH<sub>2</sub> surface groups, and an oleophobic hemisphere with either pendant alkyl / fluoroalkyl chains or Au nanoparticles, can adsorb at the air-water interface and generate aqueous foams at low particle loading (<1 wt%).<sup>57-60</sup> Polymer-functionalized JPs and bearing Au nanoparticles can also generate aqueous foams, and display a 2.2-fold increase of the catalytic activity compared to a non-foam system in the liquid-phase oxidation of D-glucose to gluconic acid.<sup>61</sup>

Herein, we disclose the high potential of amphiphilic silica JPs with oleophilic and oleophobic hemispheres and

selective spatial location of Pd nanoparticles for generating oil foams based on aromatic alcohols at low particle concentration (1 wt%) and low fluorine content (8 wt% F), and conduct selective aerobic alcohol oxidation reactions at the gas-liquid interface at ambient O<sub>2</sub> pressure. In this configuration, the gas and liquid are expected to mix directly at the G-L at the surface of particles by-coadsorption increasing their miscibility and cutting mass transfer resistances. We also report for the first time the direct visualization of the surface distribution of organic moieties on Pd/JPs using photo-induced force microscopy (PiFM), unveiling their anisotropic architecture at the nanoscale level.

## 2. RESULTS AND DISCUSSION

**2.1. Preparation and characterization of surface-active particles.** Pristine silica particles (250 nm) were synthesized by the Stöber method using tetraethyl orthosilicate (TEOS) as silica precursor, ammonium as catalyst and ethanol as solvent (**Figure S1**).<sup>62</sup> JPs (7.89 wt% F) were synthesized by the Pickering emulsion template method,<sup>63,64</sup> whereby 1H,1H,2H,2H-perfluorooctyltriethoxysilane (PFOTES) and 3-mercaptopropyltriethoxysilane (MPTES) (equimolar ratio) were sequentially grafted on silica (**Figure S2, Figure S3**, see SI for details). Besides, randomly functionalized particles (i.e. Non-JPs, 8.01 wt% F) were synthesized by concomitant grafting of PFOTES and MPTES on silica. Subsequently, Pd nanoparticles were deposited onto both particles using a modified sol-immobilization method,<sup>65</sup> yielding Pd/JPs (0.81 wt% Pd) and Pd/Non-JPs (0.82 wt% Pd), respectively (see also **Figure S4**).

Thermogravimetric analysis (TGA) was used to inspect the stability and grafting efficiency of fluorinated and mercaptopropyl chains on JPs and Non-JPs (**Figure S5a**). Both particles exhibit similar weight loss until 150 °C (~1.5%) that is attributed to water desorption. This weight loss is lower than that measured on pristine silica (~2.4%) due to its higher hydrophilicity. The total weight loss of JPs and Non-JPs particles is very similar (19% *vs.* 18%), indicating the same grafting degree of fluorinated and mercaptopropyl chains (~8 groups/nm<sup>2</sup> overall). The derivative TG curves for JPs and Non-JPs display three main peaks (**Figure S5b**): (i) a peak at 100 °C that is attributed to water desorption, (ii) a prominent peak at 300-500 °C due to the decomposition of fluorinated and mercaptopropyl chains and ethoxy groups,<sup>66</sup> and (iii) a peak between 500-600 °C that is ascribed to water release due to condensation of SiOH groups.<sup>67</sup> The derivative curve for the pristine silica also displays two peaks at 400-500 °C and 500-600 °C that are attributed to the decomposition of ethoxy groups and condensation of silanol groups, respectively.

JPs and Non-JPs were analyzed by <sup>29</sup>Si NMR MAS and <sup>13</sup>C NMR prior to Pd deposition. The <sup>29</sup>Si NMR MAS spectrum shows an intense Q<sub>4</sub> resonance band centered at 111.6 ppm that is indicative of siloxane bridges [(SiO)<sub>4</sub>Si] (**Figure S6**). An intense Q<sub>3</sub> band is also visible at -102.7 ppm together with a small Q<sub>2</sub> band at -92.2 ppm that are ascribed to Si-OH and geminal HO-Si-OH groups. A small T<sub>3</sub> band is observed at -66.5 ppm that is attributed to (SiO-)<sub>3</sub>SiR (tripodal) moieties on silica. Notably, no T<sup>1</sup> [(SiO-)<sub>3</sub>SiR(-OH)<sub>2</sub>] (monopodal) and T<sup>2</sup> [(SiO-)<sub>2</sub>SiR(-OH)] (dipodal) moieties are observed.<sup>68</sup> The <sup>13</sup>C NMR MAS spectra of JPs confirms the grafting of both fluorinated and mercaptopropyl chains (**Figure S7**). Two bands are observed at 3.8 ppm and 26.6 ppm that are attributed to CH<sub>2</sub> groups in the fluorinated and mercaptopropyl chains, respectively.<sup>69,70</sup> The bands at 19.6 and 63.5 ppm are indicative of CH<sub>3</sub> and CH<sub>2</sub> groups, respectively,

in ethoxy groups.<sup>71</sup> The bands between 110 ppm and 125 ppm are attributed to CF<sub>2</sub> and CF<sub>3</sub> groups in the fluorinated chains.<sup>69,70</sup>

The pristine silica, JPs and Non-JPs were further analyzed by FT-IR spectroscopy (**Figure 1a, Figure S8**). In all cases, two characteristic bands are visible at 1080 cm<sup>-1</sup> and 798 cm<sup>-1</sup> that are ascribed to asymmetric stretching and bending vibrations of Si-O-Si bonds, respectively.<sup>68,72</sup> A large band is also visible in the range 3000-3500 cm<sup>-1</sup> due to Si-OH groups interacting with adsorbed water. The presence of Si-OH groups is also confirmed by the asymmetric stretching vibration band centered at 950 cm<sup>-1</sup>. A tiny band is visible for Non-JPs at 1610 cm<sup>-1</sup> that can be assigned to asymmetric stretching modes of C-C groups.<sup>73</sup> No band is observed corresponding to the stretching vibration of S-H groups (2560 cm<sup>-1</sup>),<sup>74</sup> which can be explained by a low concentration of mercaptopropyl groups. Additionally, there is a broader spectral feature in the 1100-1300 cm<sup>-1</sup> range associated with weaker transverse (TO) and longitudinal optical (LO) modes. These particular modes, as previously described by Lange *et al.*, are centered at 1254, 1200, and 1170 cm<sup>-1</sup>, representing LO<sub>3</sub>, TO<sub>4</sub>, and LO<sub>4</sub> modes, respectively.<sup>75</sup> These weak bands appear as a broad shoulder, making it challenging to differentiate them. This difficulty in distinguishing bands becomes apparent when trying to assign the C-F component from PFOTES on functionalized particles, as it frequently overlaps with these silica FTIR bands. However, a subtle increase of intensity in the 1150 cm<sup>-1</sup> region for both JPs and Non-JPs samples hints the presence of C-F bond vibrations.<sup>73</sup>

To gain more insight and resolution on the C-F component, we used PiFM measurements,<sup>76</sup> taken with a penetration depth of 20 nm in the sideband acquisition mode. The local IR spectra measured by PiFM on different particle locations are congruent with the FT-IR spectra measured on the bulk samples (**Figure 1a-b**). However, unlike FT-IR which samples several micrometres into the bulk of the sample and averages over several microns laterally, PiFM mitigates against the interference from bulk SiO<sub>2</sub> frequencies and thus prevents them from obscuring the C-F component.<sup>73</sup> For pristine silica surfaces, three prominent IR components are visible at 958, 1095, and 1200 cm<sup>-1</sup> corresponding to Si-OH, Si-O-Si, and TO<sub>4</sub> vibrations, respectively (**Figure 1b**). Upon functionalization with PFOTES and MPTES, the overall intensity of the 1100-1300 cm<sup>-1</sup> region increases, with notable features at 1225 and 1320 cm<sup>-1</sup> corresponding to Si-CH<sub>2</sub> functionalities. The heightened intensity around ~1150 cm<sup>-1</sup> confirms the presence of the C-F stretching vibrations on both JPs and Non-JPs.

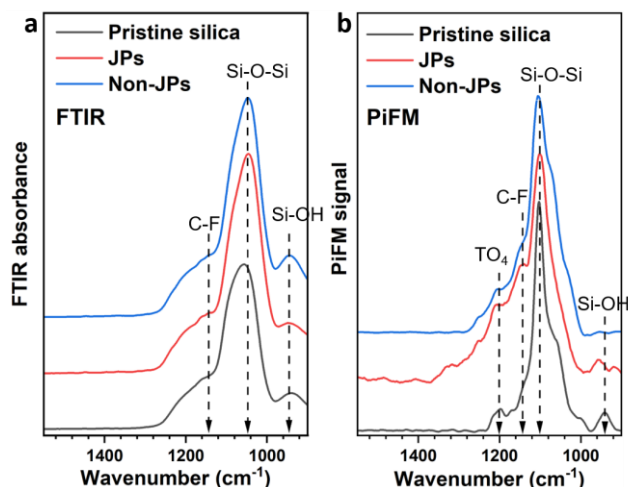


**Figure 1** (a) FT-IR and (b) PiFM spectra of pristine silica, JPs and Non-JPs. The green line indicates the location of C-F stretching vibrations.

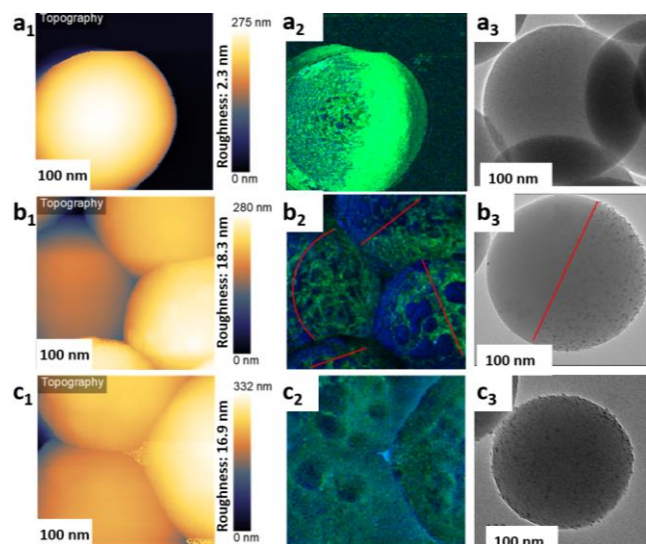


**Figure 2.** Topography, PiFM at  $1145\text{ cm}^{-1}$  and HR-TEM micrographs of (a1-a3) pristine silica, (b1-b3) Pd/JPs, and (c1-c3) Pd/Non-JPs. The dark blue and green colors in a<sub>2</sub>-c<sub>2</sub> refer to fluorocarbon chains and Si-O-Si moieties with bands at  $1145$  and  $1085\text{ cm}^{-1}$ , respectively.

The nanoscale distribution of organic moieties on the surface of pristine silica, JPs and Non-JPs was also inspected by PiFM. Pristine particles display relatively smooth surfaces with a roughness of  $2.3\text{ nm}$  (Figure 2a<sub>1</sub>). The surface roughness increases to  $18.3\text{ nm}$  and  $16.9\text{ nm}$  for JPs and Non-JPs, respectively, due to the immobilization of Pd nanoparticles [Figure 2(b<sub>1</sub>, c<sub>1</sub>)]. The anisotropic nature of JPs is clearly visible in Figure 2b<sub>2</sub> with fluorohydrocarbon chains (band at  $1145\text{ cm}^{-1}$ ) appearing in dark blue color and the Si-O-Si moieties (band at  $1085\text{ cm}^{-1}$ ) appearing in green (see also Figure 2a<sub>2</sub>). Interestingly, the intensity of fluorohydrocarbon chains is magnified by Pd nanoparticles compared to Non-JPs due to a lack of preferential Pd nanoparticle binding in the latter case (Figure 2c<sub>2</sub>). The decrease in the Si component atop Pd nanoparticles points out a spacing between the tip and silica that noticeably affects the acquisition area given the similar penetration depth of the tip compared to the

particle size. Pristine silica, JPs and non-JPs were also visualized by HR-TEM after loading with Pd (Figure 2(a<sub>3</sub>-c<sub>3</sub>)). Pd nanoparticles are clearly visible on JPs and Non-JPs. Notably, in the case of JPs, Pd nanoparticles are selectively dispersed on the thiol hemisphere (oleophilic).

X-ray photoelectron spectroscopy (XPS) was performed to analyze the Pd speciation on Pd/JPs and Pd/non-JPs (Figure S9a-f). The Pd  $3d_{5/2}$  core level can be deconvoluted into two bands centered at  $335.8\text{ eV}$  and  $337.9\text{ eV}$  that can be assigned to Pd(o) and Pd<sup>II</sup>O, respectively (Figure S9b).<sup>77,78</sup> The C1s XPS core level region shows bands at  $293.3\text{ eV}$  and  $290.9\text{ eV}$  that are assigned to CF<sub>3</sub> and CF<sub>2</sub> groups (Figure S9c-d).<sup>79</sup> The ratio of band areas for CF<sub>2</sub> and CF<sub>3</sub> groups is  $4.87$ , which is consistent with the theoretical value of  $5$ . An additional band is visible at  $288.2\text{ eV}$  that is attributed to methylene groups connected with CF<sub>2</sub>.<sup>80</sup> F 1s and S 2p core level bands are observed at  $797.8\text{ eV}$  and  $164.0\text{ eV}$ , respectively, that confirms the presence of fluorinated and mercaptopropyl chains in Pd/JPs and Pd/Non-JPs (Figure S9e,f).

**2.2. Physicochemical properties of JPs.** The interaction of particles with the gas and liquid phases can be characterized by the interfacial contact angle. The contact angles of non-metal JPs and Non-JPs particles was measured in pure BnOH, pure o-xylene and in a BnOH/o-xylene (1:1 v/v) mixture. For both particles, the contact angle decreases in the sense BnOH > mixture > and o-xylene (see Figure 3a-c for JPs and Figure 3d-f for Non-JPs). The contact angles of JPs are systematically lower than those of Non-JPs (e.g.,  $115.5^\circ$  vs.  $131.2^\circ$ ) despite the similar surface density of fluorinated chains, which is consistent with the anisotropic structure of JPs.

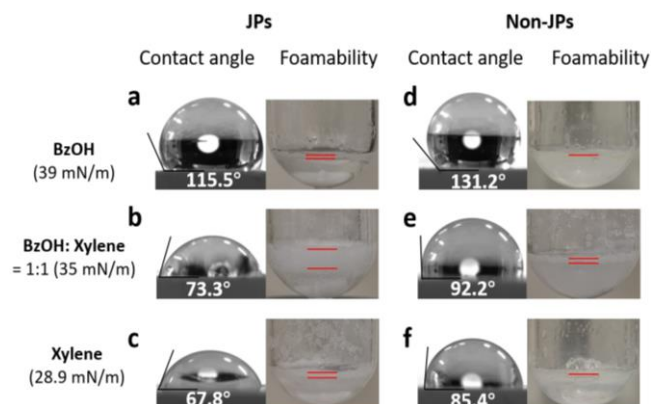


**Figure 3.** Contact angle and foamability of JPs and Non-JPs with (a, d) BnOH, (b, e) mixture, and (c, f) o-xylene, respectively. Foaming conditions:  $1.8\text{ mL}$  of solvent,  $1\text{ wt}\%$  particles,  $1500\text{ rpm}$ ,  $100\text{ }^\circ\text{C}$ ,  $1\text{ h}$ .

The foamability of metal-free JPs and Non-JPs was studied in pure BnOH, pure o-xylene and in a BnOH/o-xylene (1:1 v/v) mixture at  $100\text{ }^\circ\text{C}$  for  $1\text{ wt}\%$  particle loading using a stirring rate of  $1500\text{ rpm}$ . Both particles display no foamability in pure BnOH (surface tension =  $39\text{ mN m}^{-1}$ ) and o-xylene (surface tension =  $28.9\text{ mN m}^{-1}$ ). In contrast, JPs exhibit excellent foamability a BnOH/o-xylene (1:1 v/v) mixture (surface tension =  $35\text{ mN m}^{-1}$ ), whereas a very thin layer is formed using Non-JPs. These results point out a much stronger interfacial adsorption of JPs than Non-JPs in BnOH/o-xylene (1:1 v/v) mixture. Noteworthy, JPs exhibit foaming properties that are comparable to those of fluorinated silica particles prepared by co-precipitation, but requiring much higher fluorine content ( $25\text{-}33\text{ wt}\%$  vs.  $8\text{ wt}\%$  for JPs).<sup>81</sup> Loading of

JPs and Non-JPs with Pd nanoparticles does not alter their foamability (**Figure S10a**). The foamability (i.e. foam height) of JPs increases dramatically from 3.2 mm to 7.2 mm by increasing the particle loading from 0.5wt% to 4wt%, with concomitant decrease of the average bubble size from 355  $\mu\text{m}$  to 115  $\mu\text{m}$  (**Figure 4**). The foams show high stability for a least 48 h with minor decrease of the foam height from 5.9 mm to 4.8 mm, and increase of the average droplet size from 305  $\mu\text{m}$  to 370  $\mu\text{m}$  (1wt% JP loading) (**Figure 5**). The bubble size distributions are collected in **Figure S11**. The liquid phase is turbid just after foaming, revealing that a small fraction of particles does not adsorb at the gas-liquid interface. These particles sediment further within 3 h, leading to a clear liquid phase.

The dispersion of JPs and Non-JPs in BnOH/o-xylene mixture (1:1 v/v) was investigated by dynamic light scattering (DLS). Non-JPs display agglomeration even at very low concentration (0.001 wt%) with an average particle size of 1280 nm, and becomes more prominent at higher particle concentrations (0.01 wt% and 0.1 wt%). Agglomeration of Non-JPs is systematically larger compared to JPs which is consistent with the higher hydrophobicity of the former as inferred from their higher contact angles (**Figure S12**). The broader peak for Non-JPs reveals a higher polydispersity that can be explained by a higher hydrophobicity compared to JPs, making them more difficult to be wetted by the BnOH-xylene mixture.

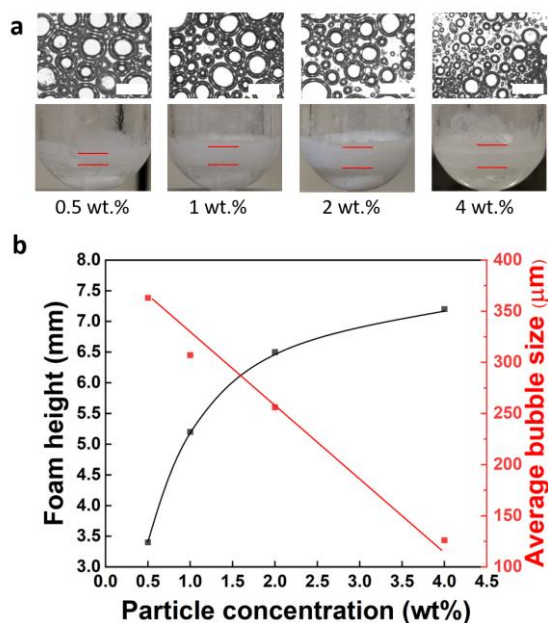


**Figure 4.** (a) Morphology and foamability of JPs in BnOH / o-xylene (1:1 v/v) mixture at room temperature and variable JP loading. The bar size is 500  $\mu\text{m}$ . (b) Evolution of the foam height (left ordinate axis) and average bubble (right ordinate axis) against the particle concentration. Foaming conditions: 0.8 mL of BnOH, 0.8 mL of o-xylene, 0.5-4.0wt% JPs, 1500 rpm, 100  $^{\circ}\text{C}$ , 1 h.

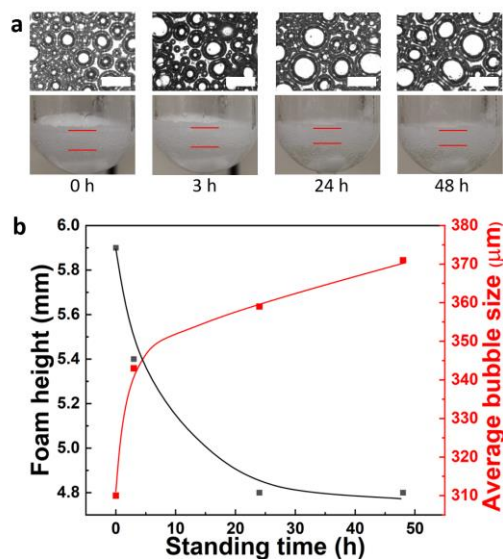


**Figure 5.** (a) Morphology and foam stability of JPs in BnOH / o-xylene (1:1 v/v) mixture at room temperature and 1wt% JP loading. The space bar size is 500  $\mu\text{m}$ . (b) Time-evolution of foam height and average bubble size. Foaming conditions: 0.8 mL of BnOH, 0.8 mL of o-xylene, 1 wt % JPs, 1500 rpm, 100  $^{\circ}\text{C}$ , 1 h, kept static at room temperature.

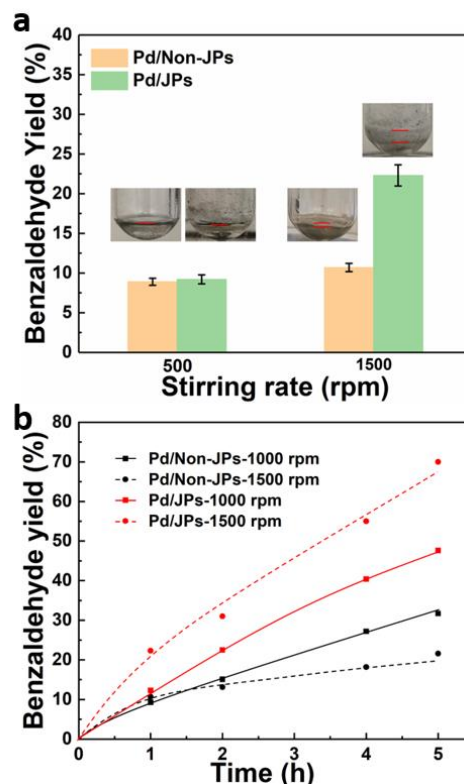


**Figure 6.** (a) Aerobic oxidation of BnOH over Pd/JPs and Pd/Non-JPs. Reaction conditions: 0.8 mL of BnOH, 0.8 mL of o-xylene,  $\text{O}_2$  balloon, 1 wt % particles, 1500 rpm, 100  $^{\circ}\text{C}$ , 1 h. (b) Kinetic profiles for the aerobic oxidation of BnOH over Pd/JPs and Pd/Non-JPs. Reaction conditions: 0.8 mL of BnOH, 0.8 mL of o-xylene,  $\text{O}_2$  balloon, 1 wt % particles, 1000 and 1500 rpm, 100  $^{\circ}\text{C}$ , variable reaction time.

To assess the surface activity of JPs and Non-JPs at the gas-liquid interface, the surface tension of BnOH/*o*-xylene mixture (1:1 v/v) was measured before and after adding JPs and Non-JPs (0.001 wt%, 0.01 wt%, and 0.1 wt%) (**Figure S13**). The results demonstrate that both particles cannot reduce the surface tension, which is consistent with previous reports.<sup>82</sup>

**2.3. Aerobic oxidation of BnOH.** With the results above, we investigated the catalytic properties of Pd/JPs and Pd/Non-JPs (1wt.%) in the aerobic oxidation of BnOH in a BnOH/*o*-xylene (1:1 v/v) mixture with/without foam (**Figure 6a**). The reaction was conducted at 100 °C for 1 h using a stirring rate of 500 rpm and 1500 rpm. Under Non-foaming conditions (500 rpm), both particles exhibit a similar benzaldehyde (BAH) yield (about 9%). However, at 1500 rpm, Pd/JPs displays a prominent increase of the BAH yield (22%), whereas it remains almost unchanged (~9%) for Pd/Non-JPs. The marked difference in the catalytic activity between both particles is attributed to the generation of abundant foam for Pd/JPs at 1500 rpm, while Pd/Non-JPs display low foamability at the same stirring rate. **Figure S14** plots the evolution of the BnOH conversion and selectivity to the different oxidation products in the aerobic oxidation reaction of BnOH over Pd/JPs and Pd/Non-JPs with and without foam, respectively, as a function of the stirring speed. For Pd/JPs particles, the BnOH conversion increases drastically from 10% to 25% when raising the stirring speed from 500 rpm to 1500 rpm. Meanwhile, the BAH selectivity increases from 86% to 92%, which can be explained by a higher O<sub>2</sub> accessibility to the active sites decreasing concomitantly the toluene selectivity by BnOH disproportionation from 11% to 7%. Opposing these observations, the BnOH conversion only increases slightly (from 10% to 12%) for Pd/Non-JPs when the stirring speed is raised from 500 rpm to 1500 rpm, whereas the BAH and toluene selectivities keep almost unchanged at 11%. Over this catalyst, the BnOH conversion increases from 12% to 17% when raising the O<sub>2</sub> pressure from 1 bar to 5 bar (maximum pressure of our reactor) (**Figure S15**). To reach the BnOH conversion obtained using Pd/JPs in foam at 1500 rpm (25%), the reaction requires a higher O<sub>2</sub> pressure, whereas the reaction in foam is operated at ambient pressure. In all cases, no benzoic acid was observed (selectivity <1%) which can be explained by radical scavenging from BnOH.<sup>83</sup> Benzyl benzoate was formed in very tiny amounts (selectivity <1%), which may come from a hemiacetal intermediate that is expected to be unstable under the reaction conditions and oxidized to the ester.<sup>84</sup>

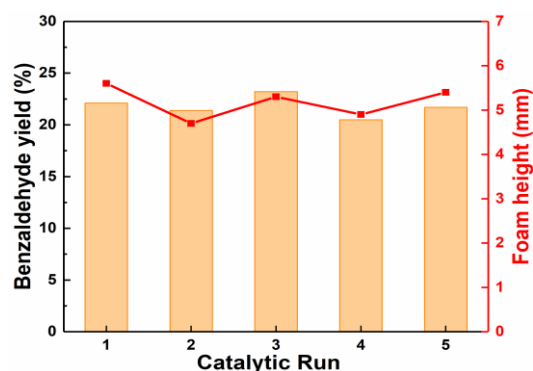
The kinetic profiles were measured for Pd/JPs and Pd/Non-JPs at 100 °C in BnOH/*o*-xylene (1:1 v/v) mixture at 1000 and 1500 rpm stirring speeds (**Figure 6b**). The BAH yield increases faster and reaches higher values after 5 h reaction over Pd/JPs compared to Pd/Non-JPs due to the formation of foam. Increasing the stirring speed from 1000 to 1500 rpm results in a prominent increase of the activity and final yield due to the higher foamability. To be noted, the BAH yields obtained over Pd/Non-JPs at 1500 rpm are lower than those measured at 1000 rpm after 2 h which can be attributed to partial catalyst sticking on the reactor wall that decreased the amount of catalyst available for the reaction. This phenomenon was not observed at 1000 rpm. From the kinetic plots, the catalytic activity at time = 0 (turnover frequency, TOF<sub>0</sub>) is 2118 h<sup>-1</sup> for Pd/JPs and 1046 h<sup>-1</sup> for Pd/Non-JPs at 1500 rpm. The TOF<sub>0</sub> keeps unchanged for

Non-JPs when changing the stirring speed from 1000 to 1500 rpm. As a result, the BAH yield reaches 70% for Pd/JP after 5 h at 1500 rpm, whereas it is only 32% for Pd/Non-JPs at 1000 rpm (used as reference). We measured the activation energies (E<sub>a</sub>) for Pd/JPs and Pd/non-JPs from the Arrhenius plots of TOF values in the temperature range of 353-383 K (**Figure S16**). The activation energy is 103 kJ/mol for Pd/Non-JPs in bulk system and decreases to 86 kJ/mol for Pd/JPs in foam system. The higher activation energy in the former case is consistent with the observation reported earlier for alcohol oxidation in aqueous foams,<sup>85</sup> and notes that it aligns with the reported findings that the activation energy for oxidation at a gas-solid interface is significantly different from that at a liquid-solid interface.<sup>86</sup> Overall, we can infer from these results that the reaction is conducted in the absence of mass transfer resistances for Pd/Non-JPs as the catalytic activity remains unchanged while varying the stirring speed. In the case Pd/JPs foaming system, the catalytic activity and selectivity increase with the stirring speed, which is attributed to a promoted gas-liquid-catalyst contact at the surface of bubbles.

**2.4. Catalyst recyclability and reuse.** We further studied the recyclability and reuse of Pd/JPs in the aerobic oxidation of BnOH for five consecutive runs. The catalytic tests were carried out at 100 °C for 1 h using 1wt% Pd/JPs. After each run, the catalytic particles were separated by centrifugation at 7200 rpm for 3 min, washed twice in acetone and dried at 80 °C for 4 h before use in the subsequent run. Pd/JPs were robust and kept their activity and foamability after each run without any significant loss (**Figure 7**). The selectivity of the reactions kept unchanging as well after recycling shown in **Figure S17**. No evidence of Pd leaching during the reaction was observed, as inferred from ICP-MS analysis of the catalysts after the 5<sup>th</sup> run (**Table S2**). Also, no Pd sintering is observed after the 5<sup>th</sup> run by comparing the size distribution of Pd nanoparticles over Pd/JPs before and after reaction (**Figure S4a-d**). This observation can be attributed to the thiol group acting as an anchor, providing stability to Pd nanoparticles.<sup>87</sup>

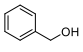
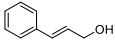
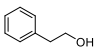
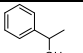
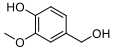
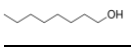
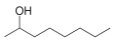
**2.5. Extension to aromatic and aliphatic alcohols.** The results above point out the much higher catalytic activity of Pd/JPs compared to Pd/Non-JPs for the aerobic oxidation of BnOH at comparable grafting degree. We then used Pd/JPs to conceive foam systems for the aerobic oxidation of aromatic alcohols under O<sub>2</sub> using 1wt% particles (**Table 1**). In particular, we designed stable foam systems for cinnamyl alcohol/*o*-xylene, 1-phenylethanol/dodecane, 2-phenylethanol/dodecane and vanillyl alcohol/dodecane mixtures, all 1:1 v/v (**Figure S10b-e**). Cinnamyl alcohol can be oxidized to cinnamaldehyde at 100°C for 1 h over Pd/JPs in foam with 34% yield (entry 2), whereas the yield is only 13% over Pd/Non-JPs in non-foam system. In the case of 1-phenylethanol, the foam system stabilized by Pd/JPs yields 6.6% phenylacetaldehyde at 120°C after 1 h reaction, whereas the non-foam system (Pd/Non-JPs) yields only 2.1% at the same conditions (entry 3). By increasing the temperature to 140°C, the yield in the non-foam system rises to 5.4%, which is still lower than the yield in the foam system at 120 °C. The twofold boost in yield is a result of the elevated kinetic energy associated with the temperature rise from 120 to 140°C. Likewise, when converting 2-phenylethanol to acetophenone, the foam system stabilized by Pd/JPs affords 14% yield at 120°C after 1 h, while the yield is only 2.1% over Pd/Non-JPs in non-foam system (entry 4). Finally, vanillyl alcohol is converted into vanillin with 34% yield at 120 °C after 1 h over Pd/JPs in foam

system, while the conversion only reaches 16% over Pd/Non-JPs without foam. Moreover, we broadened the scope from aromatic alcohols to aliphatic alcohols. Pd/JPs generated abundant foam in 1-octanol and 2-octanol and afforded higher yields for the aerobic oxidation, reaching 19.7% and 4.4%, respectively, compared to the Pd/Non-JPs system without foam, where the yields were 4.4% and 1.4%.



**Figure 7.** Recyclability and reuse of Pd/JPs for the aerobic oxidation of BnOH over five consecutive runs. Reaction conditions: 0.8 mL of BnOH, 0.8 mL of *o*-xylene, 1 wt% Pd/JPs, 1 bar O<sub>2</sub> balloon, 1500 rpm, 100 °C, 1 h.

**Table 1.** Substrate scope expansion for catalytic tests in O<sub>2</sub> atmosphere.

Reactant	Catalyst	T / °C	Solvent	System	Yield / %
	JPs	100	Xylene	Foam	23
	Non-JPs	100	Xylene	Non-foam	11
	JPs	100	Xylene	Foam	34
	Non-JPs	100	Xylene	Non-foam	13
	JPs	120	Dodecane	Foam	6.6
	Non-JPs	120	Dodecane	Non-foam	2.1
	Non-JPs	140	Dodecane	Non-foam	5.4
	JPs	120	Dodecane	Foam	14
	Non-JPs	120	Dodecane	Non-foam	6.9
	JPs	120	Dodecane	Foam	34
	Non-JPs	120	Dodecane	Non-foam	16
	JPs	140	Dodecane	Foam	19.7
	Non-JPs	140	Dodecane	Non-foam	4.7
	JPs	150	Dodecane	Foam	4.4
	Non-JPs	150	Dodecane	Non-foam	1.4

Reaction conditions: 0.8 mL substrate, 0.8 mL solvent, 1 wt% Pd/JPs catalysts, 1500 rpm, O<sub>2</sub> balloon, 1 h. (According to the Antoine equation, the partial pressure correction of O<sub>2</sub> at 100 °C in the solvent of *o*-xylene is around 0.74 bar. The partial pressure in the solvent of dodecane at 120 °C, 140 °C, and 150 °C are 0.95 bar, 0.89 bar, and 0.85 bar, respectively)

### 3. CONCLUSIONS

In summary, we prepared silica Janus particles grafted selectively with fluorinated and mercaptopropyl chains on each hemisphere, respectively, allowing tunable design of oleophobic-oleophilic properties at low fluorine content (8 wt%F). The particles were decorated with Pd nanoparticles on the oleophilic hemisphere. The anisotropic surface architecture of the particles was confirmed by pulse-induced force microscopy, allowing high resolution of fluorocarbon chains by Pd nanoparticles. Janus particles exhibited higher foamability in oil solvents compared to particles with a homogeneous surface distribution of fluorinated and mercaptopropyl chains at the same surface density of fluorinated and

mercaptopropyl groups owing to their stronger adsorption at the oil-O<sub>2</sub> interface. The catalytic performance was strongly affected by the foaming properties, and Pd-loaded Janus particles exhibited at least double yield to aldehyde/ketone products in the aerobic oxidation of aromatic alcohols compared to non-Janus particles. Extension of aromatic and aliphatic alcohols in the foam system confirms the generality of the JPs foam system. Janus particles were conveniently recycled with high foamability and catalytic efficiency maintained for at least five consecutive runs.

The results presented in this study pave the way to the design of on-purpose, adjustable oleophobic-oleophilic Janus particles to generate oil foams *à la carte* for a large variety of aromatic alcohols that could be extended to other alcohols and organic reactants by fine design of the particle hemispheres and nanoscale distribution of organic functions.

#### ASSOCIATED CONTENT

#### AUTHOR INFORMATION

#### Corresponding Author

E-mail: [peratitism@cardiff.ac.uk](mailto:peratitism@cardiff.ac.uk)

#### Notes

The authors declare no competing financial interests.

#### Supporting Information

Particle size distribution of the different particles; size distribution of Pd nanoparticles; TGA profiles, <sup>13</sup>C NMR MAS and XPS spectra and HR-TEM images of the different particles; optical images of the different kinds of aromatic alcohols in xylene foams at 100 °C after reaction; PiFM topography and spectroscopy of Janus nanoparticles. DLS results about different particles in BnOH and xylene mixture; Surface tension tests of different particles in the mixture of BnOH and *o*-xylene. This material is available free of charge via the Internet at <http://pubs.acs.org>.

#### ACKNOWLEDGEMENTS

This study was funded by the ERC grant Michelangelo (contract number #771586). AG would like to express his gratitude to the UK Catalysis Hub for funding a postdoc position (UK Catalysis Hub Consortium and funded by EPSRC grant: EP/R026939/1, EP/R026815/1, EP/R026645/1, EP/R027129/1). The PiFM spectrometer was acquired with the EPSRC grant EP/V05399X/1. The European Regional Development Fund (ERDF) and the Welsh European Funding Office (WEFO) part-funded the Cardiff Catalysis Institute Microscopy facility. XPS spectra were run by HarwellXPS, the EPSRC NRF EP/Y023552/1.

#### REFERENCES

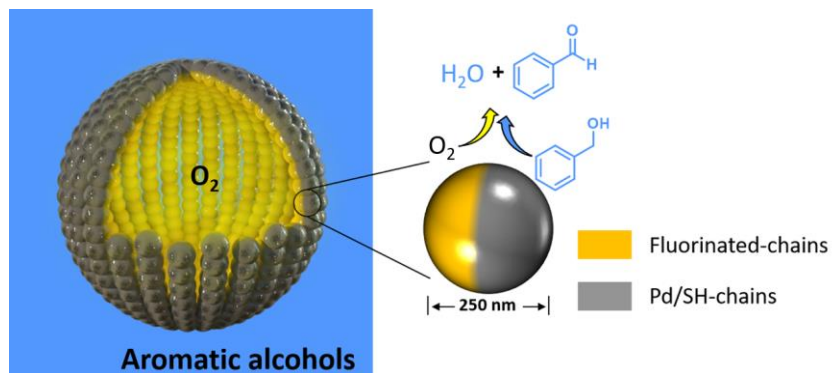
- Yekeen, N.; Manan, M. A.; Idris, A. K.; Padmanabhan, E.; Junin, R.; Samin, A. M.; Gbadamosi, A. O.; Oguamah, I. A Comprehensive Review of Experimental Studies of Nanoparticles-Stabilized Foam for Enhanced Oil Recovery. *J. Petroleum Sci. Eng.* **2018**, *164*, 43-74.
- Andrieux, S.; Quell, A.; Stubenrauch, C.; Drenckhan, W. Liquid Foam Templating—A Route to Tailor-Made Polymer Foams. *Advances Colloid Interface Sci.* **2018**, *256*, 276-290.
- Heymans, R.; Tavernier, I.; Danthine, S.; Rimaux, T.; Van der Meer, P.; Dewettinck, K. Food-Grade Monoglyceride Oil Foams: the Effect of Tempering on Foamability, Foam Stability and Rheological Properties. *Food & Function* **2018**, *9*, 3143-3154.
- Deotale, S.; Dutta, S.; Moses, J.; Balasubramaniam, V.; Anandharamakrishnan, C. Foaming Characteristics of Beverages

- and its Relevance to Food Processing. *Food Eng. Rev.* **2020**, *12*, 229-250.
- [5] Hailing, P. J.; Walstra, P. Protein-Stabilized Foams and Emulsions. *Critical Rev. Food Sci. Nutrition* **1981**, *15*, 155-203.
- [6] Rodríguez Patino, J. M.; Delgado, M. D. N.; Fernández, J. L. Stability and Mechanical Strength of Aqueous Foams Containing Food Proteins. *Colloids Surf. A* **1995**, *99*, 65-78.
- [7] Binks, B. P.; Shi, H. Aqueous Foams in the Presence of Surfactant Crystals. *Langmuir* **2020**, *36*, 991-1002.
- [8] Boos, J.; Drenckhan, W.; Stubenrauch, C. Protocol for Studying Aqueous Foams Stabilized by Surfactant Mixtures. *J. Surfactants and Detergents* **2013**, *16*, 1-12.
- [9] Robb, I. D. Specialist Surfactants, Springer Science & Business Media, **1996**; (b) Bergeron, V.; Hanssen, J. E.; Shoghl, F. Thin-Film Forces in Hydrocarbon Foam Films and Their Application to Gas-Blocking Foams in Enhanced Oil Recovery. *Colloids Surf. A* **1997**, *123*, 609-622.
- [10] Bauget, F.; Langevin, D.; Lenormand, R. Dynamic Surface Properties of Asphaltenes and Resins at the Oil-Air Interface. *J. Colloid Interface Sci.* **2011**, *239*, 501-508.
- [11] Blázquez, C.; Emond, E.; Schneider, S.; Dalmazzone, C.; Bergeron, V. Non-Aqueous and Crude Oil Foams. *Oil & Gas Sci. Technol.* **2014**, *69*, 467-479.
- [12] Shrestha, L. K.; Aramaki, K.; Kato, H.; Takase, Y.; Kunieda, H. Foaming Properties of Monoglycerol Fatty Acid Esters in Nonpolar Oil Systems. *Langmuir* **2006**, *22*, 8337-8345.
- [13] Binks, B. P. Particles as Surfactants – Similarities and Differences. *Curr. Opinion Colloid Interface Sci.* **2002**, *7*, 21-41.
- [14] Hunter, T. N.; Pugh, R. J.; Franks, G. V.; Jameson, G. J. The Role of Particles in Stabilising Foams and Emulsions. *Adv. Colloid Interface Sci.* **2008**, *137*, 57-81.
- [15] Murakami, R.; Bismarck, A. Particle-Stabilized Materials: Dry Oils and (Polymerized) Non-Aqueous Foams. *Adv. Funct. Mater.* **2010**, *20*, 732-737.
- [16] Binks, B. P.; Rocher, A. Stabilisation of Liquid-Air Surfaces by Particles of Low Surface Energy. *Phys. Chem. Chem. Phys.* **2010**, *12*, 9169-9171.
- [17] Binks, B. P.; Rocher, A.; Kirkland, M. Oil Foams Stabilised Solely by Particles. *Soft Matter* **2011**, *7*, 1800-1808.
- [18] Binks, B. P.; Tyowua, A. T. Influence of the Degree of Fluorination on the Behaviour of Silica Particles at Air-Oil Surfaces. *Soft Matter* **2013**, *9*, 834-845.
- [19] Binks, B. P.; Sekine, T.; Tyowua, A. T. Dry Oil Powders and Oil Foams Stabilised by Fluorinated Clay Platelet Particles. *Soft Matter* **2014**, *10*, 578-589.
- [20] Lai, Y.; Zhou, H.; Zhang, Z.; Tang, Y.; Ho, J. W. C.; Huang, J.; Tay, Q.; Zhang, K.; Chen, Z.; Binks, B. P. Multifunctional TiO<sub>2</sub>-Based Particles: The Effect of Fluorination Degree and Liquid Surface Tension on Wetting Behavior. *Part. Part. Syst. Charact.* **2015**, *32*, 355-363.
- [21] Binks, B. P.; Johnston, S. K.; Sekine, T.; Tyowua, A. T. Particles at Oil-Air Surfaces: Powdered Oil, Liquid Oil Marbles, and Oil Foam. *ACS Appl. Mater. Interfaces* **2015**, *7*, 14328-14337.
- [22] Dyab, A. K. F.; Al-Haque, H. N. Particle-Stabilised Non-Aqueous Systems. *RSC Adv.* **2013**, *3*, 13101-13105.
- [23] Fameau, A. L.; Saint-Jalmes, A. Non-Aqueous Foams: Current Understanding on the Formation and Stability Mechanisms. *Adv. Colloid Interface Sci.* **2017**, *247*, 454-464.
- [24] de Gennes, P. G. *Soft Matter. Rev. Mod. Phys.* **1992**, *64*, 645-648.
- [25] Jiang, S.; Chen, Q.; Tripathy, M.; Luijten, E.; Schweizer, K. S.; Granick, S. Janus Particle Synthesis and Assembly. *Adv. Mater.* **2010**, *22*, 1060-1071.
- [26] Walther, A.; Müller, A. H. E. Janus Particles: Synthesis, Self-Assembly, Physical Properties, and Applications. *Chem. Rev.* **2013**, *113*, 5194-5261.
- [27] Poggi, E.; Gohy, J.-F. Janus Particles: From Synthesis to Application. *Colloid Pol. Sci.* **2017**, *295*, 2083-2108.
- [28] Kirillova, A.; Marschelke, C.; Synytska, A. Hybrid Janus Particles: Challenges and Opportunities for the Design of Active Functional Interfaces and Surfaces. *ACS Appl. Mater. Interfaces* **2019**, *11*, 9643-9671.
- [29] Binks, B. P.; Fletcher, P. D. I. Particles Adsorbed at the Oil-Water Interface: A Theoretical Comparison Between Spheres of Uniform Wettability and "Janus" Particles. *Langmuir* **2001**, *17*, 4708-4710.
- [30] Cheung, D. L.; Bon, S. A. F. Stability of Janus Nanoparticles at Fluid Interfaces. *Soft Matter* **2009**, *5*, 3969-3976.
- [31] Aveyard, R. Can Janus Particles Give Thermodynamically Stable Pickering Emulsions? *Soft Matter* **2012**, *8*, 5233-5240.
- [32] Correia E. L.; Brown N.; Razavi S. Janus Particles at Fluid Interfaces: Stability and Interfacial Rheology. *Nanomaterials* **2021**, *11*, 1-29.
- [33] Kim, J. W.; Cho, J.; Cho, J.; Park, B. J.; Kim, Y.-J.; Choi, K.-H.; Kim, J. W. Synthesis of Monodisperse Bi-Compartmentalized Amphiphilic Janus Microparticles for Tailored Assembly at the Oil-Water Interface. *Angew. Chem. Int. Ed* **2016**, *55*, 4509-4513.
- [34] Kim, J.-W.; Lee, D.; Shum, H. C.; Weitz, D. A. Colloid Surfactants for Emulsion Stabilization. *Adv. Mater.* **2008**, *20*, 3239-3243.
- [35] Mejia, A. F.; Diaz, A.; Pulella, S.; Chang, Y. W.; Simonetty, M.; Carpenter, C.; Batteas, J. D.; Mannan, M. S.; Clearfield, A.; Cheng, Z. Pickering Emulsions Stabilized by Amphiphilic Nanosheets. *Soft Matter* **2012**, *8*, 10245-10253.
- [36] Ruhland, T. M.; Gröschel, A. H.; Ballard, N.; Skelton, T. S.; Walther, A.; Müller, A. H. E.; Bon, S. A. F. Influence of Janus Particle Shape on their Interfacial Behavior at Liquid-Liquid Interfaces. *Langmuir* **2013**, *29*, 1388-1394.
- [37] Tanaka T.; Okayama M.; Minami H.; Okubo M. Dual Stimuli-Responsive "Mushroom-Like" Janus Polymer Particles as Surfactants Particulate. *Langmuir* **2010**, *26*, 11732-11736.
- [38] Passas-Lagos, E.; Schüth, F. Amphiphilic Pickering Emulsifiers Based on Mushroom-Type Janus Particles. *Langmuir* **2015**, *31*, 7749-7757.
- [39] Koike R.; Iwashita Y.; Kimura Y. Emulsion Droplets Stabilized by Close-Packed Janus Regular Polygonal Particles. *Langmuir* **2018**, *34*, 12394-12400.
- [40] de Folter, J. W. J.; Hutter, E. M.; Castillo, S. I. R.; Klop, K. E.; Philipse, A. P.; Kegel, W. K. Particle Shape Anisotropy in Pickering Emulsions: Cubes and Peanuts. *Langmuir* **2014**, *30*, 955-964.
- [41] Chen C.; Zhang L.; Wang N.; Sun D.; Yang Z. Janus Composite Particles and Interfacial Catalysis Thereby. *Macromol. Rapid Commun.* **2023**, doi: <https://doi.org/10.1002/marc.202300280>.
- [42] Glaser, N.; Adams, D. J.; Böker, A.; Krausch, G. Janus Particles at Liquid-Liquid Interfaces. *Langmuir* **2006**, *22*(12), 5227-5229.
- [43] Faria, J.; Ruiz, M. P.; Resasco, D. E. Phase-Selective Catalysis in Emulsions Stabilized by Janus Silica-Nanoparticles. *Adv. Synth. Catal.* **2010**, *352*, 2359-2364.
- [44] Greydanus, B.; Schwartz, D. K.; Medlin, J. W. Controlling Catalyst-Phase Selectivity in Complex Mixtures with Amphiphilic Janus Particles. *ACS Appl. Mater. Interfaces* **2019**, *12*, 2338-2345.
- [45] Zhao, T.; Zhu, X.; Hung, C.-T.; Wang, P.; Elzatahry, A.; Al-Khalaf, A. A.; Hozzein, W. N.; Zhang, F.; Li, X.; Zhao, D. Spatial Isolation of Carbon and Silica in a Single Janus Mesoporous Nanoparticle with Tunable Amphiphilicity. *J. Am. Chem. Soc.* **2018**, *140*, 10009-10015.
- [46] Li D.-D.; Jiang J.-Z.; Cai C. Palladium Nanoparticles Anchored on Amphiphilic Janus-Type Cellulose Nanocrystals for Pickering Interfacial Catalysis. *Chem. Commun.* **2020**, *56*, 9396-9399.
- [47] Yan, S.; Zou, H.; Chen, S.; Xue, N.; Yang, H. Janus Mesoporous Silica Nanosheets with Perpendicular Mesochannels: Affording Highly Accessible Reaction Interfaces for Enhanced Biphasic Catalysis. *Chem. Commun.* **2018**, *54*, 10455-10458.
- [48] Ifra; Thodikayil, A. T.; Saha, S. Compositionally Anisotropic Colloidal Surfactant Decorated with Dual Metallic Nanoparticles as a Pickering Emulsion Stabilizer and Their Application in Catalysis. *ACS Appl. Mater. Interfaces* **2022**, *14*, 23436-23451.
- [49] Dou, S.-Y.; Wang, R. The C-Si Janus Nanoparticles with Supported Phosphotungstic Active Component for Pickering Emulsion Desulfurization of Fuel Oil without Stirring. *Chem. Eng. J.* **2019**, *369*, 64-76.
- [50] Kirillova, A.; Schliebe, C.; Stoychev, G.; Jakob, A.; Lang, H.; Synytska, A. Hybrid Hairy Janus Particles Decorated with Metallic Nanoparticles for Catalytic Applications. *ACS Appl. Mater. Interfaces* **2015**, *7*, 21224-21225.
- [51] Zhao, R.; Han, T.; Sun, D.; Huang, L.; Liang, F.; Liu, Z. Poly(ionic liquid)-Modified Magnetic Janus Particles for Dye Degradation. *Langmuir* **2019**, *35*, 11435-11442.
- [52] Zhou Y.; Shen F.; Zhang S.; Zhao Q.; Xu Z.; Chen H. Synthesis of Methyl-Capped TiO<sub>2</sub>-SiO<sub>2</sub> Janus Pickering Emulsifiers for Selective Photodegradation of Water-Soluble Dyes. *ACS Appl. Mater. Interfaces* **2020**, *12*, 29876-29882.

- [53] Wang B.; Li K.; Yan J.; Zhou T. Synthesis of Functionalized Janus Hybrid Nanosheets for One-Step Construction of Pickering Emulsion and Selective Photodegradation of Water-Soluble Dyes. *Colloids Surf. A*, **2023**, *664*, 131199.
- [54] Bu, E.; Chen, Y.; Wang, C.; Cheng, Z.; Luo, X.; Shu, R.; Zhang, J.; Liao, M.; Jiang, Z.; Song, Q. Hydrogen Production from Bio-Derived Biphasic Photoreforming over a Raspberry-Like Amphiphilic Ag<sub>2</sub>O-TiO<sub>2</sub>/SiO<sub>2</sub> Catalyst. *Chem. Eng. J.* **2019**, *370*, 646-657.
- [55] Wang, C.; Zhong, W.; Peng, S.; Zhang, J.; Shu, R.; Tian, Z.; Song, Q.; Chen, Y. Robust Hydrogen Production via Pickering Interfacial Catalytic Photoreforming of n-Octanol-Water Biphasic System. *Frontiers Chem.* **2021**, *9*, 712453.
- [56] Chang, F.; Vis, C. M.; Bergmeijer, M.; Howes, S. C.; Bruijninx, P. C. A. Bifunctional Janus Silica Spheres for Pickering Interfacial Tandem Catalysis. *ChemSusChem*. **2021**, *14*, 5328-5335.
- [57] Wang, K.; Wang, G.; Lu, C.; Wang, Y. Preparation of Amphiphilic Janus Particles and their Application in Stabilising Foams. *Micro Nano Lett.* **2018**, *13*, 397-402.
- [58] Fujii, S.; Yokoyama, Y.; Nakayama, S.; Ito, M.; Yusa, S-I.; Nakamura, Y. Gas Bubbles Stabilized by Janus Particles with Varying Hydrophilic-Hydrophobic Surface Characteristics. *Langmuir* **2018**, *34*, 933-942.
- [59] Wang, G.; Wang, K.; Wang, Y. Synthesis of Amphiphilic Fluorinated Janus Particles with Applications in Stabilizing Surfactant-Free Foams. *Particuology* **2018**, *41*, 112-117.
- [60] Yang, L.; Wang, T.; Yang, X.; Jiang, G.; Luckham, P.F.; Xu, J.; Li, X.; Ni, X. Highly Stabilized Foam by Adding Amphiphilic Janus Particles for Drilling a High-Temperature and High-Calcium Geothermal Well. *Ind. Eng. Chem. Res.* **2019**, *58*, 9795-9805.
- [61] Frank, B. D.; Perovic, M.; Djalali, S.; Antonietti, M.; Oschatz, M.; Zeininger, L. Synthesis of Polymer Janus Particles with Tunable Wettability Profiles as Potent Solid Surfactants to Promote Gas Delivery in Aqueous Reaction Media. *ACS Appl. Mater. Interfaces* **2021**, *13*, 32510-32519.
- [62] Stöber, W.; Fink, A.; Bohn, E. Controlled Growth of Monodisperse Silica Spheres in the Micron Size Range. *J. Colloid Interface Sci.* **1968**, *26*, 62-69.
- [63] Hong, L.; Jiang, S.; Granick, S., Simple Method to Produce Janus Colloidal Particles in Large Quantity. *Langmuir* **2006**, *22*, 9495-9499.
- [64] Perro, A.; Meunier, F.; Schmitt, V.; Ravaine, S., Production of Large Quantities of "Janus" Nanoparticles Using Wax-in-Water Emulsions. *Colloids Surf. A* **2009**, *332*, 57-62.
- [65] Villa, A.; Wang, D.; Veith, G. M.; Vindigni, F.; Prati, L. Sol Immobilization Technique: a Delicate Balance Between Activity, Selectivity and Stability of Gold Catalysts. *Catal. Sci. Technol.* **2013**, *3*, 3036-3041.
- [66] Pardal, F.; Lapinte, V.; Robin, J. J. Modification of Silica Nanoparticles by Grafting of Copolymers Containing Organosilane and Fluorine Moieties. *J. Pol. Sci. Part A: Pol. Chem.* **2009**, *47*, 4617-4628.
- [67] Kunc, F.; Balhara, V.; Sun, Y.; Daroszewska, M.; Jakubek, Z. J.; Hill, M.; Brinkmann, A.; Johnston, L. J. Quantification of Surface Functional Groups on Silica Nanoparticles: Comparison of Thermogravimetric Analysis and Quantitative NMR. *Analyst* **2019**, *144*, 5589-5599.
- [68] Cui, J.; Chatterjee, P.; Slowing, I. I.; Kobayashi, T. In Situ <sup>29</sup>Si Solid-State NMR Study of Grafting of Organoalkoxysilanes to Mesoporous Silica Nanoparticles. *Micropor. Mesopor. Mater.* **2022**, *339*, 112019.
- [69] Chen, Q.; Schmidt-Rohr, K. <sup>19</sup>F and <sup>13</sup>C NMR Signal Assignment and Analysis in a Perfluorinated Ionomer (Nafion) by Two-Dimensional Solid-State NMR. *Macromolecules* **2004**, *37*, 5995-6003.
- [70] Ashu-Arrah, B. A.; Glennon, J. D.; Albert, K. Synthesis and Characterization of Bonded Mercaptopropyl Silica Intermediate Stationary Phases Prepared Using Multifunctional Carbon Dioxide as a Reaction Solvent. *J. Chromatography A* **2020**, *1222*, 38-45.
- [71] Li, Y.; Zhao, G.; Hong, B.; Zhao, S-L.; Han, X.; Pera-Titus, M. Unraveling Particle Size and Roughness Effects on the Interfacial Catalytic Properties of Pickering Emulsions. *Colloids & Surf A* **2020**, *599*, 124800.
- [72] Chukin, G. D.; Malevich, V. I. Infrared Spectra of Silica. *J. Appl. Spectroscopy* **1977**, *26*, 223-229.
- [73] Shahabadi, S. M. S.; Rabiee, H.; Seyed, S. M.; Mokhtare, A.; Brant, A. Superhydrophobic Dual Layer Functionalized Titanium Dioxide/Polyvinylidene Fluoride-co-Hexafluoropropylene (TiO<sub>2</sub>/PH) Nanofibrous Membrane for High Flux Membrane Distillation. *J. Membr. Sci.* **2017**, *537*, 140-150.
- [74] Senkevich, J. J.; Mitchell, C. J.; Yang, G-R.; Lu, T-M. Surface Chemistry of Mercaptan and Growth of Pyridine Short-Chain Alkoxy Silane Molecular Layers. *Langmuir* **2002**, *18*, 1587-1594.
- [75] Lange, P.; Windbracke, W. Characterization of Thermal and Deposited Thin Oxide Layers by Longitudinal Optical-Transverse Optical Excitation in Fourier Transform IR Transmission Measurements. *Thin Solid Films*, **1989**, *174*, 159-164.
- [76] Sifat A. A.; Jahng J.; Potma E. O. Photo-Induced Force Microscopy (PIFM)—Principles and Implementations. *Chem. Soc. Rev.* **2022**, *51*, 4208-4222.
- [77] Kim, K. S.; Gossmann, A.; Winograd, N. X-Ray Photoelectron Spectroscopic Studies of Palladium Oxides and the Palladium-Oxygen Electrode. *Anal. Chem.* **1974**, *46*, 197-200;
- [78] Kibis, L.; Titkov, A.; Stadnichenko, A.; Koscheev, S.; Boronin, A. X-Ray Photoelectron Spectroscopy Study of Pd Oxidation by RF Discharge in Oxygen. *Appl. Surf. Sci.* **2009**, *255*, 9248-9254.
- [79] Zhu, X. L.; Liu, S. B.; Man, B. Y.; Xie, C. Q.; Chen, D. P.; Wang, D. Q.; Ye, T. C.; Liu, M. Analysis by Using X-Ray Photoelectron Spectroscopy for Polymethyl Methacrylate and polytetrafluoroethylene Etched by KrF Excimer Laser. *Appl. Surf. Sci.* **2007**, *253*, 3122-3126.
- [80] Lee, Y. S. Syntheses and Properties of Fluorinated Carbon Materials. *J. Fluorine Chem.* **2007**, *128*, 392-403.
- [81] Zhang, S.; Dedovets, D.; Feng, A.; Wang, K.; Pera-Titus, M. Pickering Interfacial Catalysis for Aerobic Alcohol Oxidation in Oil Foams. *J. Am. Chem. Soc.* **2022**, *144*, 1729-1738.
- [82] Kotula, A. P.; Anna, S. L. Probing Timescales for Colloidal Particle Adsorption Using Slug Bubbles in Rectangular Microchannels. *Soft Matter* **2012**, *8*, 10759-10772.
- [83] Sankar, M.; Nowicka, E.; Carter, E.; Murphy, D. M.; Knight, D. W.; Bethell, D.; Hutchings G. J. The Benzaldehyde Oxidation Paradox Explained by the Interception of Peroxy Radical by Benzyl Alcohol. *Nat. Commun.* **2014**, *5*, 3332.
- [84] Li, G.; Enache, D. I.; Edwards, J.; Carley, A. F.; Knight, D. W.; Hutchings, G. J. Solvent-Free Oxidation of Benzyl Alcohol with Oxygen Using Zeolite-Supported Au and Au-Pd Catalysts. *Catal. Lett.* **2006**, *110*, 7-13.
- [85] Huang, J.; Cheng, F.; Binks, B. P.; Yang, H. pH-Responsive Gas-Water-Solid Interface for Multiphase Catalysis. *J. Am. Chem. Soc.* **2015**, *137*, 15015-15025.
- [86] Wang, H.; Sapi, A.; Thompson, C. M.; Liu, F.; Zherebetskyy, D.; Krier, J. M.; Carl, L. M.; Cai, X.; Wang, L. W.; Somorjai, G. A. J. Am. Chem. Soc. **2014**, *136*, 10515-10520.
- [87] Huang, P.; Zeng, X.; Du, F.; Zhang, L.; Peng, X. Palladium Nanoparticles Anchored on Thiol Functionalized Xylose Hydrochar Microspheres: An Efficient Heterogeneous Catalyst for Suzuki Cross-Coupling Reactions. *Catal. Lett.* **2020**, *150*, 1011-1019.



TOC graphic specifications.



Insert Table of Contents artwork here